

# Reduction of CCD Observations Made with the Fabry-Perot Scanning Interferometer. II. Additional Procedures

A.V. Moiseev<sup>1</sup> and O.V.Egorov<sup>2</sup>

<sup>1</sup> Special Astrophysical Observatory Russian Academy of Sciences, N. Arkhyz, KChR, 369167, Russia

<sup>2</sup> Sternberg Astronomical Institute, Universitetskii pr. 13, Moscow, 119992 Russia

November 12, 2007/Revised: November 20, 2007

**Abstract.** We describe a software package used at the Special Astrophysical Observatory of the Russian Academy of Sciences to reduce and analyze the data obtained with the Fabry-Perot scanning interferometer. We already described most of the algorithms employed in our earlier Paper I (Moiseev, 2002). In this paper we focus on extra procedures required in the case of the use of a high-resolution Fabry-Perot interferometer: removal of ghosts and measurement of the velocity dispersion of ionized gas in galactic and extragalactic objects.

## 1. Introduction

Scanning Fabry-Perot interferometer (FPI) can be used to perform a detailed analysis of the structure and kinematics of galaxies, nebulae, and other extended objects. Detailed descriptions of the main idea of this observational method and references to earlier papers can be found in Moiseev (2002) (hereafter Paper I) and Gordon et al. (2000). The result of observations has the form of a set of two-dimensional interferograms—the convolution of the monochromatic image of the object with the transmission curve of the FPI at each step of scanning. After special reduction (phase-shift correction) these interferograms can be assembled into a “data cube”. In such a cube, each spatial element in the detector plane is associated with its individual spectrum. The spectral interval is usually not very wide and amounts to only 5–50 Å, making it possible to study, e.g., the kinematics of ionized gas, based on the data for one or two emission lines.

To reduce observational data obtained with the FPI, one needs appropriate software, which differs from the software employed to analyze the data obtained with slit spectrographs. Paper I gives a brief review of the systems commonly used to reduce such data. Of the recently published papers on the subject we point out the paper by Daigle et al. (2006) who suggested a number of new procedures: adaptive spatial binning of data cubes prior to constructing the velocity fields, algorithms for detecting emission lines and subtraction of night-sky lines.

At the Special Astrophysical Observatory of the Russian Academy of Sciences (SAO RAS) the scanning FPI is a part of the CCD-based SCORPIO multimode

focal reducer (Afanasiev & Moiseev, 2005). Unlike two-dimensional photon counters, which made a return recently and are now used in combination with the FPI (Gach et al., 2002), “slower” CCDs require a different kind of algorithms to reduce the data obtained. This concerns, first and foremost, photometric correction of channels and night-sky spectrum subtraction. We addressed this issue in detail in our earlier Paper I, where we described the algorithms used in the software to reduce SCORPIO observations performed in the scanning FPI mode.

According to ASPID<sup>1</sup> database, a total of about 180 FPI data cubes have been obtained with the 6-m telescope of SAO RAS in 2000–2007, with at least 30 publications based on these data. The experience in the reduction of this observational data allowed us to improve our software package and develop a number of new useful procedures for data analysis. In this paper we focus on describing these procedures. In section 2 we address the problem of removing the ghost light, which arises in high-resolution FPIs, in section 3 we consider the problem of velocity dispersion measurements and in section 4 briefly describe the software package currently employed to reduce observations made with the 6-m telescope using the scanning FPI incorporated into SCORPIO instrument.

## 2. Ghosts subtraction

SCORPIO is now equipped with two scanning interferometers (hereafter referred to as IFP235 and IFP501) with a gap between the plates corresponding to 235 and 501 orders of interference, respectively, at the wavelength of  $\lambda 6562.8\text{\AA}$ . See Paper I for detailed parameters of both

Send offprint requests to: A.V. Moiseev, e-mail: moisav@sao.ru

<sup>1</sup> <http://alcor.sao.ru/db/aspid/>

interferometers. Because of the FPI location in the output pupil of the system between the collimator and the camera of the focal reducer ghost lights appear on the image. Ghost lights are due to backlight reflecting inside the interferometer plates and between these plates and the nearest lenses of the focal reducer, surfaces of the narrow-band filter, etc. This is a well known problem, and various ghost “families” were described by Bland-Hawthorn (1995), and a somewhat more detailed description can be found in the paper by Jones et al. (2002). Putting IFP235 into the beam produces ghosts so that the main image and these ghosts are aligned symmetrically with respect to the optical axis of the FPI. The intensity of these ghost reflections (which we refer to as “diametral ghosts”, “D”, in accordance with the ghost classification suggested by Bland-Hawthorn (1995) and Jones et al., 2002) amounts to about 10% of the intensity of the main image. In such cases it is usually recommended to tilt the FPI with respect to the optical axis of the system so as to move the ghost outside the detector field. However, certain design features of SCORPIO focal reducer prevent the use of this option. Therefore during observations the image of the object should be placed off the optical axis, and care must be taken to ensure that ghosts from field stars do not fall on the object of interest. All these problems decrease the working field of view of SCORPIO focal reducer by a factor of two.

In observations made with IFP501 another—“exponential” (“E”, according to the terminology of Bland-Hawthorn (1995) and Jones et al., 2002)—family of ghost images appears. These ghost images form as a result of back reflections inside the plates of the FPI and pose a more serious problem than diametral ghosts, because the nearest exponential ghost is located within only  $16''$  of the object image, and its intensity is rather high (about 12% of the brightness of the object). Such intense ghost images are due to the degradation of the antireflective coating of the outer surfaces of the IFP501 plates. Unfortunately, the cost of plate replacement (or recoating) in this case is close to that of assembling a new FPI, which is rather high. We nevertheless were tempted to use IFP501 before a new interferometer was acquired, because the former performs well in terms of other characteristics—first and foremost, because of its  $R \approx 8300$  spectral resolution at the  $H_\alpha$  line wavelength, which is rather high for extragalactic astronomy. Such an instrument proved to be very popular among the observers at the 6-m telescope for tasks that are impossible to perform with IFP235 because of its lower spectral resolution. These were primarily observations of nebulae with relatively small (within 100–200 km/s) range of radial velocities: Herbig–Haro objects, star-forming regions in the Milky Way and other galaxies, etc.

In a number of cases ghost traces can be removed at the stage of data reduction by applying the appropriate algorithms. Figure 1 (whose idea we borrowed from Bland-Hawthorn (1995) and Jones et al., 2002) clearly illustrates the complex pattern of ghost images. Namely, the image

of the galaxy (G) produces closely-spaced ghost images  $E_0G$  and  $E_1G$  whose brightness is equal to 4% and 12% of the object brightness, respectively. Now,  $E_1G$  produces  $E_2G$ , which, in turn, produces  $E_3G$ —and the brightness of these ghosts is equal to 1.4% and 0.15% of the brightness of G, i.e., the brightness of ghosts decreases exponentially as it must be in the case of multiple reflections. These ghosts appear at the front plate of the FPI before light passes through the interferometer, and therefore are referred to as monochromatic—their relative intensity in the data cube does not change with wavelength  $\lambda$ . At the same time, ghost  $E_0G$  appears at the back plate of the FPI after interference has taken place. The image of such a ghost on the interferogram is located in a domain corresponding to other wavelengths. Hence the data cube should exhibit an offset in  $\lambda$  between the spectra of G and  $E_0G$ , and it must depend on the position of the image on the detector.

In Fig. 1 we also indicate diametral ghosts, i.e., ghosts located symmetrically with respect to the optical axis of the interferometer. The image of galaxy G and the corresponding ghost DG are located symmetrically with respect to the optical axis, ghost  $E_1G$  produces diametral ghost  $DE_1G$ , and ghost  $E_2G$ , respectively, produces  $DE_2G$ , etc. Ghost DG also generates a family of secondary exponential ghosts:  $E_1DG$  can be seen in the figure. The latter is superposed by diametral ghost  $DE_0G$ . Diametral ghosts have rather complex structure, as is immediately apparent in the case of ghost DS produced by the brightest foreground star. Namely, this ghost consists of two images of the star—a normal image (with the intensity equal to  $\sim 5\%$  of that of star S) and a strongly defocused image, which has the shape of a ring, whose total intensity is equal to about 10% of intensity S.

Note that it is by no means always possible to find so many ghost images as in Fig. 1. The figure illustrates a limit case corresponding to observations of a relatively bright object, whereas usually only the brightest ghosts (DG,  $E_0G$ , and  $E_1G$ ) can be seen. We describe the pattern of ghost images in such detail, because we believe that our analysis will help the users better understand the data obtained and distinguish real emission features from ghosts.

If we denote the ideal data cube (i.e., the cube without ghosts) as  $I_{real}$ , then the wavelength-calibrated observed cube has the following form:

$$I_{obs}(x, y, \lambda) = I_{real}(x, y, \lambda) + I_{ghost}(x, y, \lambda), \quad (1)$$

where the family of exponential ghosts can be represented in the form:

$$I_{ghost}(x, y, \lambda) \approx f_0 \hat{P} I_{real}^{-1}(x - \Delta x_0, y - \Delta y_0, z) + \sum_{i=1}^{i_{max}} f_i I_{real}(x - \Delta x_i, y - \Delta y_i, \lambda). \quad (2)$$

Relative brightness  $f_i$  of ghosts decreases exponentially with the number  $i$  of reflections and therefore summation is performed not to infinity, but up to  $i_{max} = 3 - 5$ , because the contribution of higher-order ghosts is usually

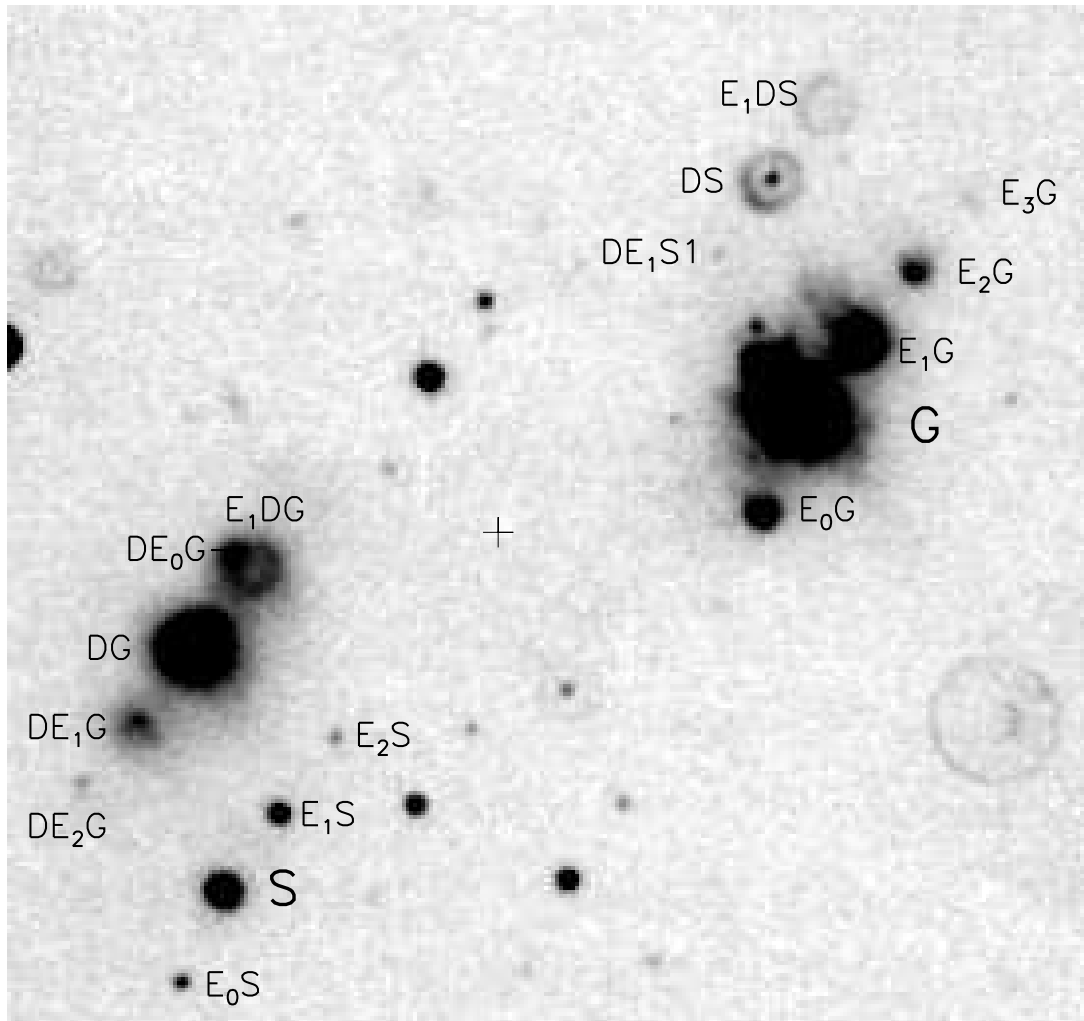


**Fig. 1.** Examples of ghost images produced in the IFP501 interferometer. H $\alpha$  observations were performed on January 30/31, 2007 at the request of C. Muñoz-Tuñón. Here “G” and “S” denote the II Zw 70 galaxy and a bright foreground star, respectively. The sum of all channels in the data cube is shown. Diametral and exponential ghost images are denoted by “D” and “E”, respectively. The cross indicates the center of the field of view.

insignificant. For the same reason, we neglect the contribution of secondary ghosts, such as non-monochromatic satellites of the ghosts of the monochromatic family. The first term in (2) describes the wavelength-shifted ghost  $E_0G$ . Here  $\hat{P}$  denotes “phase correction”, i.e., the transformation from spectra expressed in terms of the FPI channel numbers  $z$  to spectra expressed in terms of the wavelengths:

$$I(x, y, \lambda) = \hat{P}I(x, y, z) = I(x, y, k(z + p(x, y))),$$

where  $p(x, y)$  is the so-called phase map (see Section 2 in Paper I for details), and  $k(z) = k_1z + k_0$  is a linear function whose coefficients are determined by the particular FPI employed. Correspondingly,  $I_{real}^{-1}$  is a result of the reverse transformation from wavelength scale to the scale of interferometer channels:

$$I_{real}^{-1}(x, y, z) = \hat{P}^{-1}I_{real}(x, y, \lambda).$$

Our aim is to infer from  $I_{obs}$  the best approximation to ghost-cleaned cube  $I_{real}$ . We use the following iterative

procedure for this. We substitute  $I_{obs}$  for  $I_{real}$  in formula (2) to obtain the first approximation to the ghost model  $I_{ghost}^1(I_{real})$ . In this case, the first approximation to the ghost-cleaned cube has, according to formula (1), the following form:  $I_{real}^1 = I_{obs} - I_{ghost}^1$ . We now substitute  $I_{real}^1$  into formula (2) to derive the following approximation to ghost model  $I_{ghost}^2$ , etc., up to  $I_{ghost}^n$ . Because of the small relative brightness of ghost images ( $f_i \ll 1$ ), only a few iterations ( $n = 3-4$ ) are needed to construct a close-to-reality ghost-image model.

The following relations are true for the family of monochromatic ghost images ( $i \geq 1$ ):

$$\Delta x_i = i\Delta x_1, \quad \Delta y_i = i\Delta y_1, \quad f_i = f^i,$$

and hence model (2) has only six free parameters, which are chosen in a way to minimize the differences between  $I_{ghost}^n$  and  $I_{obs}$ . The following table gives the mean values of these parameters, which vary little from night to night.

Our experience in the reduction of the data obtained with IFP501 shows that the model based on the above

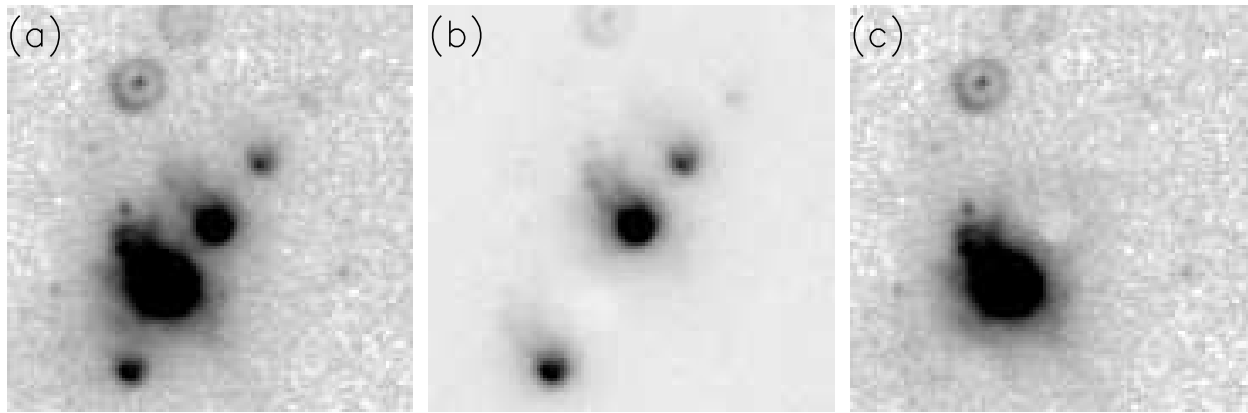


**Fig. 2.** Subtraction of ghost images. Here we show the sum of all channels of the data cube for the II Zw 70 galaxy: (a) initial image, (b) model of brightness distribution in ghost images, and (c) the result of subtracting the model from the initial cube.

**Table 1.** Parameters of ghost-image model in H $\alpha$  line

	$i = 0$	$i = 1$
$f_i$	0.038	0.11
$\Delta x_i, ''$	-7.67	9.80
$\Delta y_i, ''$	-16.42	13.63

algorithm usually describes real ghost images rather well, with no appreciable bias. The only exception are the data obtained under unstable atmospheric conditions, when counts in individual channels had to be averaged in order to compensate for appreciable (more than 10–20%) variations of the FWHM of stellar images (for a description of photometric correction see Paper I).

Figure 2 shows how the ghosts around the image of the dwarf galaxy II Zw 70 are subtracted. Other examples of observational data processed using the above deghostification procedure can be found, e.g., in Lozinskaya et al. (2003,2006) – a study of star-forming regions in the dwarf galaxies IC1613 and VII Zw403, Martínez-Delgado et al. (2007) – kinematics of ionized gas in blue compact galaxies, Movsessian et al. (2007) – study of outflows from young stellar objects in the HL/HX Tau region.

Yet another problem arises in observations of objects with strong surface-brightness gradients, where an intense ghost of, e.g., the galaxy nucleus, projects onto regions of much lower brightness. The level of Poisson noise is determined by the combined intensity of the ghost and the base. Therefore after the subtraction of the ghost model a situation may arise where the useful signal in the region considered is comparable to the amplitude of photon noise. To avoid loss of spectral information from low-brightness regions in observations of such objects, we recommend to divide the planned exposure into two and perform observations successively with two different orientations of the instrument’s field of view turned by about 90° in position angle. The ghosts obtained in the two data cubes should then project onto different regions of the object. After primary reduction, the corresponding ghost model is subtracted from each data cube and the regions are

masked where the signal-to-noise ratio decreased strongly after ghost removal. The two cubes are then combined into one and spectra of masked regions in each cube are substituted by the corresponding “good” spectra from the other data set. One of the best examples of application of the above algorithm is the reduction of observations of the nearby dwarf galaxy IC 10 reported by Lozinskaya et al. (2008). Here the image of emission shells of ionized gas occupies more than half of the entire field of view of SCORPIO instrument. Figure 3 illustrates the sequence of operations in the process of subtracting ghosts from the images of these galaxy.

### 3. Velocity dispersion measurement

A number of observational programs performed with the FPI (e.g., mapping the ionized-gas velocity dispersion in galaxies) require accurate estimates of the halfwidths of emission lines. These estimates must take into account the broadening due to the instrumental profile. It is common practice to use the following formula (which assumes that both the instrumental profile of the spectrograph and the initial—unbroadened—line profile can be described by Gaussian functions with the dispersions equal to  $\sigma_{real}$  and  $\sigma_{ins}$ , respectively):

$$\sigma_{obs} = \sqrt{\sigma_{real}^2 + \sigma_{ins}^2}. \quad (3)$$

Here  $\sigma_{obs}$  denotes the dispersion of the Gaussian used to describe the profile of the line observed at the output of the instrument. Hereafter by measuring the velocity dispersion we mean estimating  $\sigma_{real}$  from the observed spectra. One should keep in mind that broadening of lines in the spectrum of the observed object may be caused not only by velocity dispersion  $\sigma_{gas}$  (the measure of chaotic motions along the line of sight), but also by a number of other factors. Thus, according to Rozas et al. (2000), the following formula can be written for the integrated spectrum of HII regions:

$$\sigma_{real}^2 = \sigma_{gas}^2 + \sigma_N^2 + \sigma_{tr}^2, \quad (4)$$

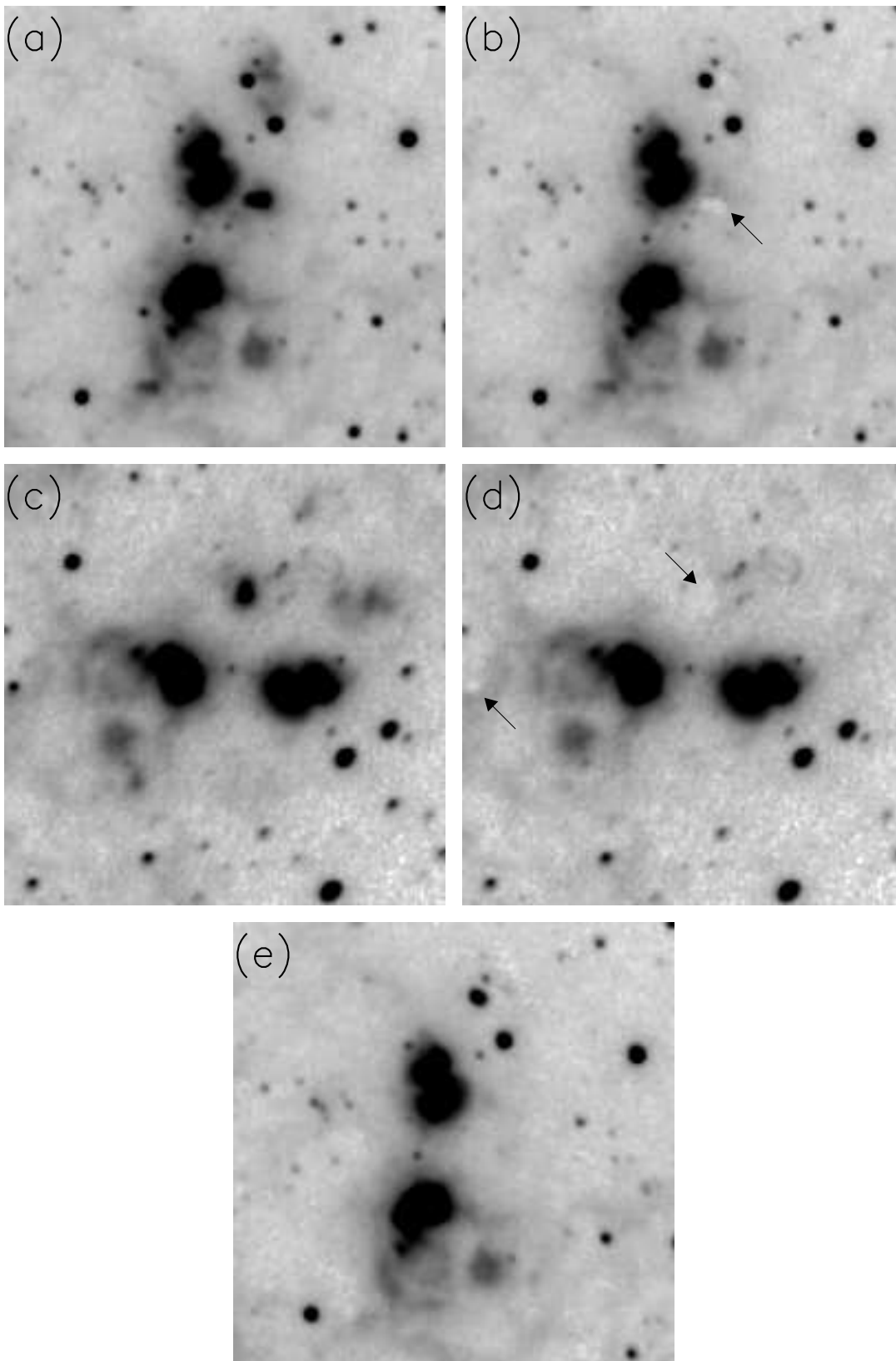


**Fig. 3.** Sum of channels in the data cubes for the IC 10 galaxy.  $H\alpha$ -line observations were made on September 8/9, 2005 at the request of T. A. Lozinskaya. The figure shows a  $72'' \times 72''$  fragment of the image. (a) Initial image in the first cube; (b) the image after ghost subtraction, the arrow indicates regions with unsatisfactory quality of subtraction; (c) the image in the cube obtained by turning the field of view by  $90^\circ$ ; (d) subtraction of ghosts from the second cube (the arrows indicate low-quality regions), and (e) the combinations of the two data cubes.

where  $\sigma_N^2 \approx 3$  km/s and  $\sigma_{tr}^2 \approx 9.1$  km/s correspond to the natural width of the emission line and its thermal broadening at  $10^4$  K, respectively.

Because of its simple and self-explanatory form, formula (3) is widely used to analyze spectroscopic data. It is often generalized by substituting FWHM for  $\sigma$ . However, one must keep in mind that exact equality in (3) is achieved only for Gaussian functions, because a convolution of two Gaussians is also a Gaussian. The assumption about the Gaussian form of the instrumental profile is usually true for slit spectrographs. However, the instrumental profile of the FPI, which is given by the Airy function, has wide wings and is best approximated by a Lorentz profile (see, e.g., Bland-Hawthorn (1995) and Paper I) rather than by a Gaussian. Therefore if the initial profile of the emission line is a Gaussian with the dispersion determined by formula (4), then the observed profile is the convolution of the Gaussian and Lorentz profiles and is hence given by the Voigt function:

$$V(\lambda, y) = \frac{1}{\sqrt{2\pi}\sigma_{real}} \frac{y}{\pi} \int_{-\infty}^{\infty} \frac{e^{-x^2} dx}{y^2 + (a - x)^2}, \quad (5)$$

where

$$a = \frac{\lambda - \lambda_0}{\sqrt{2}\sigma_{real}}, \quad y = \frac{w_{ins}}{\sqrt{2}\sigma_{real}}.$$

Here  $\lambda_0$  is the central wavelength and  $w_{ins}$  denotes the halfwidth of the instrumental (Lorentz) profile of the FPI as determined from the spectrum of the lines of the calibration lamp. We then approximate the observed profile by function (5) to obtain the required estimate  $\sigma_{real}$ . It is evident from Fig. 4 that compared to the Gaussian the Voigt profile fits much better the line wings in the galaxy spectra observed with IFP501. It is clear from general considerations that formula (5) is a more correct tool for estimating the velocity dispersion than formula (3). In the latter case we have to use Gaussian approximation for the profiles of the lines that deviate systematically from the adopted approximation (Fig. 4a), and this may introduce an additional error in the estimated  $\sigma_{real}$ . However, this approach is highly popular in velocity-dispersion measurements for extragalactic HII regions (see, e.g., Martínez-Delgado, 2007; Muñoz-Tuñón, 1995; Rozas et al. 2000). We believe that this method owes its popularity not only to the less complex appearance of formula (3) compared to that of formula (5), but also to the fact that Gaussian approximation of spectral-line profiles is incorporated into virtually all packages of astronomical data reduction. The use of the Voigt profile for analyzing extragalactic spectra is less common (see, e.g., 1994), despite the fact that integration in (5) poses no problem for modern computers.

We estimated the errors of measurement of the kinematical parameters (radial velocity and velocity dispersion) for both approaches considered. We smoothed the instrumental profile of the FPI by a Gaussian with the dispersion equal to  $\sigma_{in}$  and then added noise to the resulting spectrum and estimated the velocity dispersion using

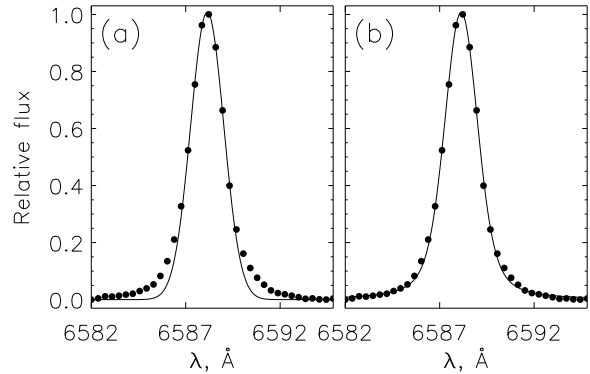


**Fig. 4.** Example of the H $\alpha$ -line spectral profile in the II Zw 70 galaxy based on observations with IFP501 (dots). The solid line shows Gaussian (a) and Voigt (b) fits.

both methods. The difference between the output ( $\sigma_{out}$ ) and input ( $\sigma_{in}$ ) velocity dispersions allows us to estimate the error  $\sigma_{err}$  of the velocity dispersion measuring. We obtained a total of 1000 independent measurements for each fixed signal-to-noise ratio ( $S/N$ ). We similarly estimated the error of measured radial velocity. We performed our computations for the instrumental profiles with the width near the H $\alpha$  line equal to  $w_{ins} = 35$  and  $w_{ins} = 115$  km/s for IFP501 and IFP235, respectively. Figures 5 (a, b) and 6 (a, b) show the results of computations—radial-velocity and velocity-dispersion errors as functions of the signal level. As expected, the error of radial-velocity measurements for symmetric lines does not depend on the algorithm employed. At the  $S/N = 30$  it is equal to 2.5 and 8 km/s for interferometers IFP501 and IFP235, respectively.

The situation is quite different for the error of the measured velocity dispersion. As expected, the error of measurements based on Voigt-profile fits smoothly decreases with decreasing signal level and amounts to only several km/s for  $S/N > 20$ . These errors are due to noise in the measured spectra and they contain no systematic component. Contrariwise, if measurements are based on relation (3) then systematic but not random component of measurement error starts to dominate at  $S/N \geq 10$ . More specifically, velocity dispersion is overestimated, as it is evident from Figs. 5c and 6c. Velocity-dispersion estimates inferred from Gaussian fits to the profiles exceed the actual values by 7–8 and 20–25 km/s for IFP501 and IFP235, respectively. Such a systematic error is unimportant for estimating widths of lines with  $\sigma_{real} > 100$  km/s. However, velocity dispersion may be overestimated by up to 100% in the case  $\sigma_{real} = 10 - 20$  km/s. This may be of critical importance, e.g., in the studies of ionized gas in star-forming regions, when it is necessary to identify expanding shells or regions where the velocities of chaotic motions exceed the speed of sound in the interstellar medium (Martínez-Delgado et al. 2007; Relaño & Beckman, 2005). In these cases velocity dispersion estimates inferred by fitting the Voigt profile are to be used. Or, if for some reasons the authors prefer Gaussian approximation, it is necessary to

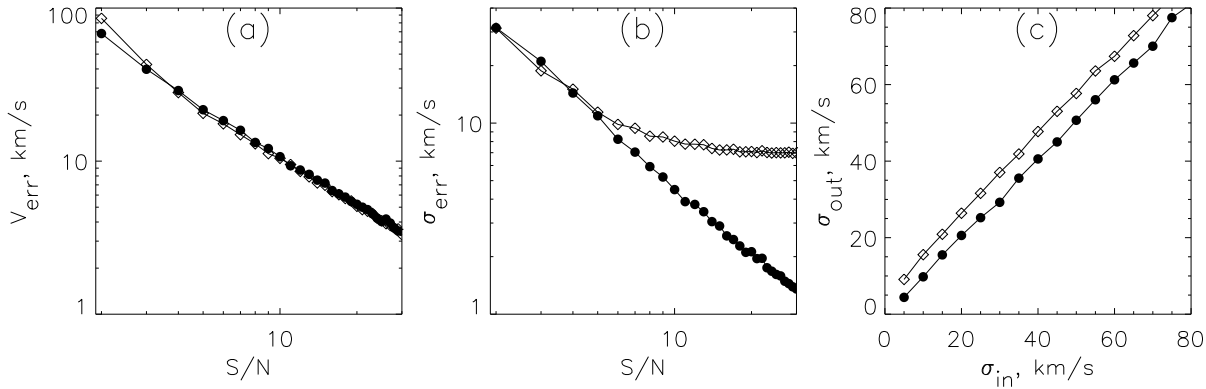


**Fig. 5.** Simulation of errors of measurement of kinematic parameters (at the  $1\sigma$  level). The computations were made for IFP501. The diamond signs and filled circles show the Gaussian and Voigt-profile approximations, respectively. (a) Dependence of the error of radial-velocity measurements on the signal-to-noise ratio. The average velocity dispersion was equal to 50 km/s; (b) error of measured velocity dispersion as a function of signal-to-noise ratio under the same conditions; (c) comparison of the initial and measured velocity dispersion (for  $S/N = 20$ ).

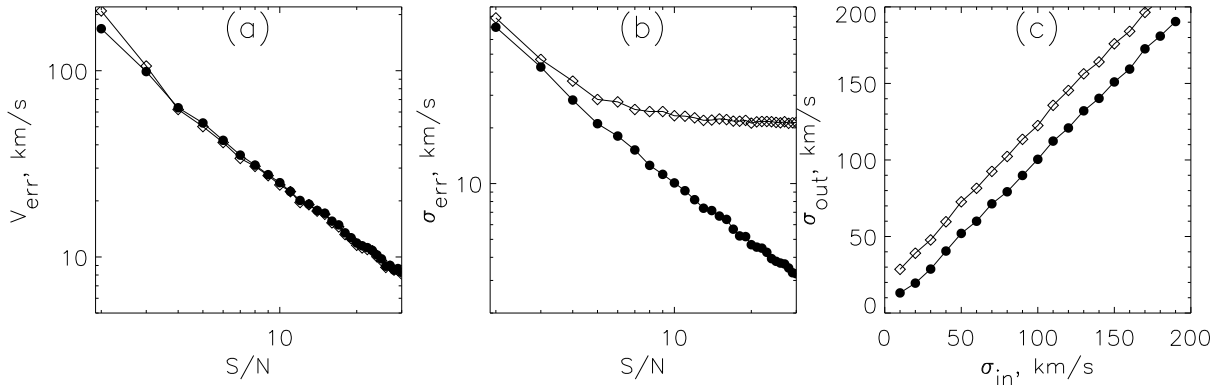


**Fig. 6.** Same as Fig. 5, but for IFP235. Figures (a) and (b) are for the case where an average velocity dispersion is equal to 200 km/s.

estimate systematic errors like we did it above and correct correspondingly the estimates based on formula (3).

Note that Relaño & Beckman (2005) proposed an alternative method to account for the instrumental profile of the FPI using the reconstruction (deconvolution) technique. This procedure is to be used for multicomponent lines. However, the method can be applied only to spectra with sufficiently high signal-to-noise ratios.

#### 4. Brief description of the software package

To reduce observations made with the FPI on SCORPIO, we wrote IFPWID program package with multi-window user-friendly interface in IDL 6.X language (Fig. 7). The codes are publicly available at <http://www.sao.ru/hq/moisav/soft>. Below in this section we describe the principal sequence of data-reduction steps to be made when using these programs. We do not describe in detail most of the algorithms employed—wavelength-scale calibration, photometric correction, night-sky line subtraction, etc. (see our sufficiently

detailed Paper I, and only briefly list the initial data for the reduction of a set of CCD frames:

- *OBJECT*—interferograms of the object studied.
- *NEON*—images of interference rings from the emission line selected by the narrow-band filter from the spectrum of the He-Ne-Ar calibration lamp. This calibration is usually performed before and after the observing night.
- *FLAT*—interferograms of uniform “flat-field” illumination produced by the continuous-spectrum lamp and obtained with the same narrow-band filter as was used for observations of the object.
- *TEST*—images of the rings from the line-spectrum lamp in some FPI channels obtained along with object integrations at the same position of the telescope. These images are used to monitor the accuracy of scanning and to control the offset of the center of the rings due to the instrument flexures.

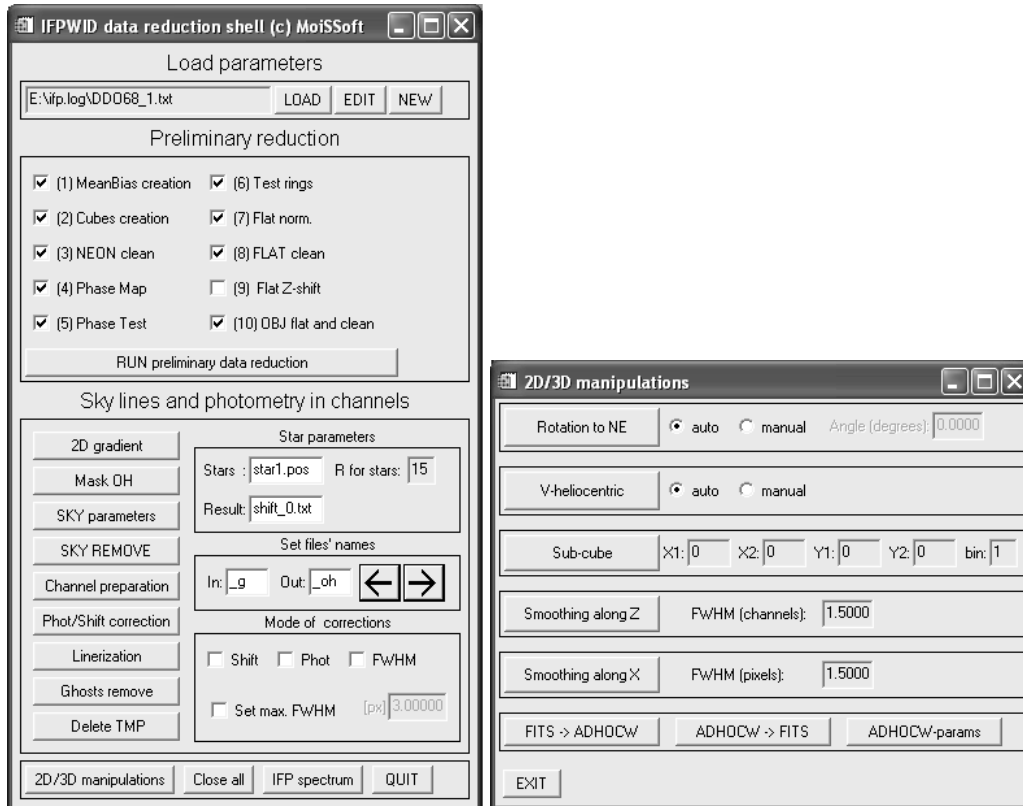


**Fig. 7.** IFPWD interface: the main menu (on the left) and the menu of operations with calibrated cubes (on the right).

#### 4.1. Assembling the Data Cubes

The first stage of reduction usually requires no special settings. As a rule, it suffices to indicate only the number of the observational night, file-name templates, and the required frame format (some observations with the FPI involve the readout of only a fragment of the CCD). The program extracts all the remaining necessary information (parameters of the FPI, numbers of spectral channels, etc.) from the descriptors of the corresponding FITS files, which are filled automatically in the process of observations. Therefore the user only has to check the required reduction steps in the menu (see the upper part of the menu in Fig. 7) and press the “run” button. Below we briefly list these steps (their names used in the reduction program are italicized):

- Search for and averaging of the bias-current frames taken in the required mode of CCD readout (*MeanBias creation*). The resulting superbias frame is then subtracted from all object integration and calibration frames. The CCD employed contains virtually no “hot” pixels, dark current is small and therefore can be neglected for exposures about several minutes.
- Creation of data cubes from individual frames (*Cubes creation*). Superbias is subtracted and bad columns are masked. Further operations are the reduction of three-dimensional cubes (object interferograms and calibration data assembled in order of channels). Cubes are stored in the standard FITS format (NAXIS=3).
- Removal of cosmic-ray hits from the cubes of calibrating-lamp integration with line (*NEON clean*) and continuous (*FLAT clean*) spectra. Simple  $\sigma$ -filter is used here: the counts in the spectra that deviate from the mean by more than preset threshold value are substituted by the half-sum of the neighboring channels.
- Construction of the phase-shift map based on the results of Lorentz-profile fits to the lines in the NEON cube (*Phase map*). A correction is applied, where necessary, to allow for nonuniform scanning of the calibrating cube (see Paper I).
- Testing the accuracy of wavelength scale (*Phase test*). The NEON cube is corrected for the phase shift and then the position of the emission line of the calibration lamp is measured for each pixel.
- Computation of corrections to the wavelength scale constructed from the calibration cube (*Test rings*). The offsets (along both coordinates in the CCD plane and along the wavelength coordinate) of TEST frames are computed relative to the NEON cube (to correct for the instrument flexures and to monitor the scanning accuracy of the FPI).
- Correction (if needed) of relative variations of FLAT lamp brightness during scanning of the calibration cube (*Flat norm*).



- Measurement of the offsets between the transmission maxima of the narrow-band filter measured for the FLAT cube and for the spectra of selected stars in the field of the object (*Flat Z-shift*). This procedure is usually needed only for observations made with IFP235, where the half-width of the narrow-band filter is appreciably smaller than the wavelength interval between the neighboring orders of interference. The offset is usually close to zero, however, it may reach 2–3.5 Å for some filters.
- Division of the cube by the flat-field (to correct for the transmission curve of the narrow-band filter) and cosmic-ray hit removal (*OBJ flat and clean*).

#### 4.2. Subtraction of Night-Sky Lines and Conversion to the Wavelength Scale

Then comes the turn of the reduction procedures that require the user’s intervention more often than during the stage of assembling the data cubes. The procedures correspond to the buttons of the main interface (the left-hand part of Fig. 7a), which are italicized below. Reduction is usually performed in the following order:

- Correction for the background gradient (*2D gradient*). In case of observations of objects in some narrow-band filters the background brightness distribution in the object cube exhibits appreciable gradient even after the division by the FLAT, especially in the presence of additional light pollution due to the Moon. This residual gradient must be due to nonuniform illumination from the FLAT lamp combined with specifics of the interference coatings of particular filters. The user can correct this effect by setting the parameters of the two-dimensional brightness distribution to which the object cube is normalized.
- Creation of the mask for subtracting the spectrum of the night sky (*Mask OH*). The mask is based on the image of the sum of the channels of the object cube. Regions with the brightness below the given threshold are considered as “background”. The resulting mask can be edited if necessary.
- Setting the parameters for the sky-background subtraction (*SKY parameters*). We described our technique of sky-background subtraction in the Paper I. Its main idea is to average sky background emission in each channel of the OBJ cube over the azimuthal angle within narrow rings centered on the optical axis of the FPI with taking into account the mask constructed at the previous stage of reduction. The average brightness profile is then subtracted from the interferogram of the object. The user may choose various modes of such subtraction, vary the width of the rings where averaging is performed, fix the center of the rings or set options for an automatic search of the ring center in each channel. When needed, averaging can be performed within individual sectors (such a procedure can

be useful for correcting for variations of the instrumental contour over the field of view), etc.

- Subtraction of the night-sky spectrum in accordance with the parameters given above (*Sky remove*).
- Photometry of stars in each channel of the object cube (*Channels preparation*). The relative offsets of the image centers, variations of FWHM and integral flux are measured for stars from a precompiled list and the averaged dependences of these parameters on the number of the channel in the cube are constructed.
- Photometric correction of the object cube based on the results of photometry of stars in each individual channel (*Photo/Shift corrections*). Corrective channel offsets are applied and account is taken of variations of atmospheric transparency (the channel counts are multiplied by the computed coefficients) and seeing (convolution with two-dimensional Gaussians).
- Conversion of the object cube to the wavelength scale (*Linearization*).
- Subtraction of ghosts using the procedure described in Section 2 (*Ghosts remove*).

#### 4.3. Processing of Calibrated Cubes

The reduction steps described above produce a wavelength-calibrated data cube with maximum account taken of all instrumental effects. In this form it can be analyzed using various software tools depending on the user preferences or on the task to be accomplished. The data can also be converted to the format adopted in the popular ADHOC<sup>2</sup> reduction system. Below we describe the operating sequence to be performed with our software tools in order to map emission-line radial-velocity and velocity-dispersion distributions.

Figure 7 (on the right) shows the menu of operations with calibrated cubes. The following procedures (their names are italicized) are performed:

- Rotation of the cube to the “correct” orientation of the images (with North at the top and East on the left), because observations can be performed at any arbitrary (or specially selected) position angle (*Rotation to NE*). The turn angle is computed from the data of the descriptors of the FITS-file header to within 0.1°. In the cases where better accuracy is required astrometric reduction is to be performed using field stars.
- Correcting the radial velocities for the motion of the Earth about the Sun (*V-heliocentric*). The necessary information is extracted from the FITS-file header.
- If necessary, a cube fragment is cut containing the object studied (*Sub-cube*). In this form reduced FPI cubes are usually stored in our ASPID database 1.
- Smoothing the cubes using a one- and two-dimensional Gaussians of given width along the spec-

<sup>2</sup> ADHOC software package was developed by J. Boulesteix (Observatoire de Marseille) and is available at <http://www.oamp.fr/adhoc/adhocw.htm>

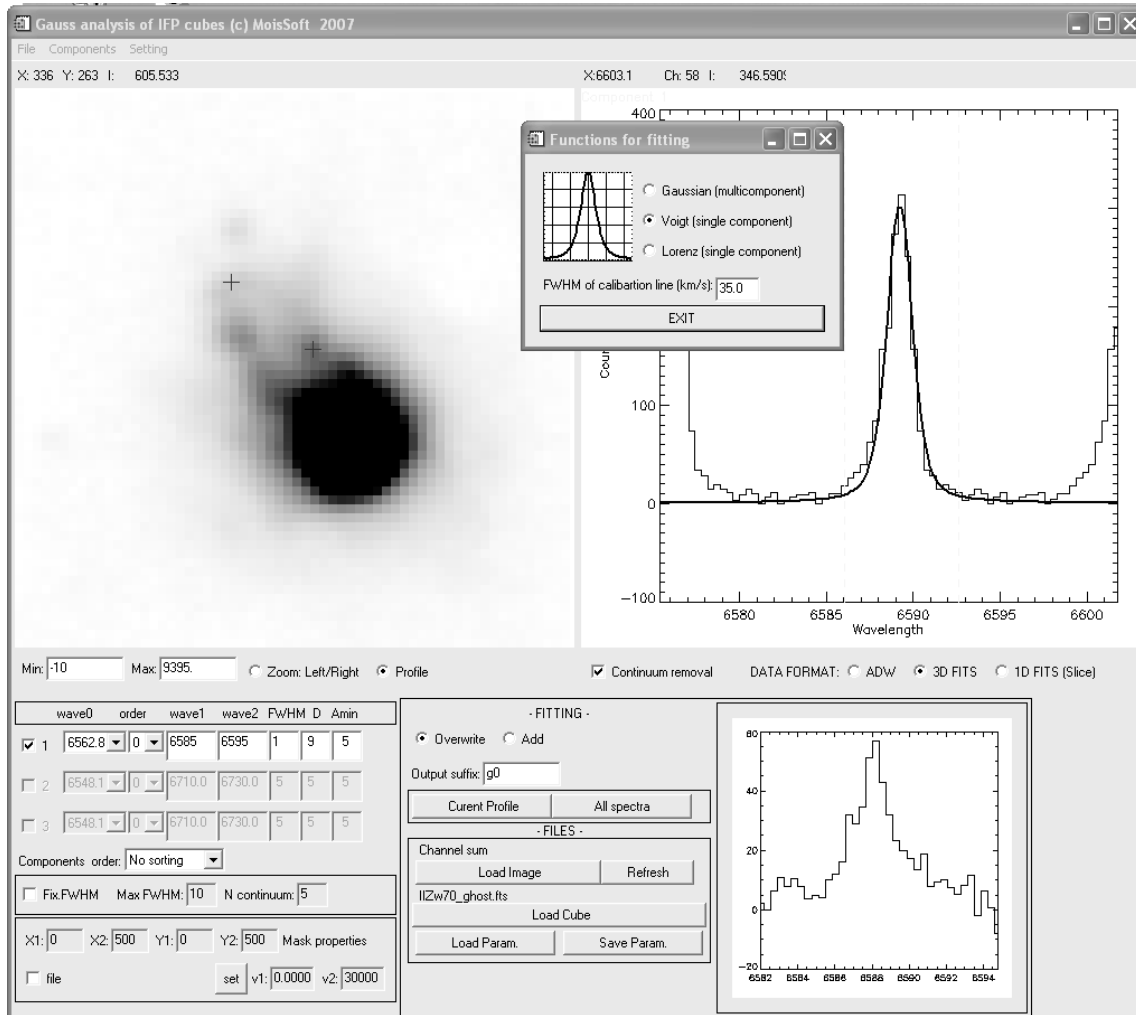


**Fig. 8.** Interface of the program of the analysis of emission-line profiles.

tral (*Smoothing along Z*) and spatial (*Smoothing along X*) coordinates, respectively.

We construct the velocity fields, velocity-dispersion maps, monochromatic images in the emission line and in the continuum, using GAUS program whose main interface is shown in Fig. 8. This program can be used to analyze individual profiles in selected pixels of the data cube by fitting the emission-line profiles to Voigt and Gauss functions. The integral in (5) is computed via standard VOIGT function of the IDL language. The main task performed by the program is an automatic identification of emission lines in the data cube and their approximation by various functions for the given parameters. This is important because the number of pixels that contain useful signal in our data cubes may amount to several hundred thousands, thereby preventing individual approach to each spectrum. Our procedure yields two-dimensional maps of profile parameters (Doppler velocities, line fluxes, etc.).

## 5. Conclusions

In this paper we briefly describe the software currently used to reduce observations made with the scanning FPI operated as a part of SCORPIO instrument. We believe the software complex described here to fully meet the requirements imposed by the research tasks performed at the 6-m telescope of the SAO RAS using the observational technique considered. In our opinion, further evolution of the data reduction software package should be associated with project of the development of SCORPIO-2 new-generation multimode focal reducer at the SAO RAS. We hope, first and foremost, that the new illuminator of the calibration beam would make it possible to abandon flat-field correction procedures (nonuniform residual background, FLAT cube wavelength shift observed in some narrow-band filters etc.). Higher automation level of SCORPIO-2 (compared to the current version of the instrument) will allow further unification of the process of acquisition data with the FPI and manage without “manual” setting of parameters in a number of procedures. The latter primarily concerns subtraction of the night-sky spectrum. In this case it will suffice to simply

develop a pipeline for the reduction of the data obtained with the scanning FPI.

*Acknowledgements.* We are grateful to A. A. Smirnova for her assistance in the preparation of the text. This work was supported by the Russian Foundation for Basic Research (project no. 06-02-16825) and a grant of the President of the Russian Federation (project MK1310.2007.2).

## References

- Afanasiev V.L., Moiseev A.V., 2005, *Astronomy Letters*, **31**, 193; astro-ph/0502095
- Bland-Hawthorn J., 1995, in *Proceedings of IAU Colloquium 149 on Tridimensional Optical Spectroscopic Methods in Astrophysics, Marseille, France, 1994*, Eds. by G. Comte, and M. Marcellin, (ASP Conference Series, San Francisco, 1995), 72
- Chilingarian I., Afanasiev V., Bonnarel F., et al., 2007, in *Proceeding of the Conference on Astronomical Data Analysis Software and Systems XVI, Tucson, USA, 2006*, Eds. by R.A. Shaw, F. Hill, and D.J. Bell, (ASP Conference Series, 2007), 271; arXiv:0711.0341 [astro-ph]
- Daigle O., Carignan C., Hernandez O., et al., 2006, *MNRAS* **368**, 1016
- Gach J.-L., Hernandez O., Boulesteix J., et al., 2002, *PASP* **114**, 1043
- Gebhardt K., C. Pryor, T. B. Williams, and J. E. Hesser, *AJ* **107**, 2067 (1994).
- Gordon S., Koribalski B., Houghton S., Jones K., 2000, *MNRAS* **315**, 248
- Jones D.H., Shopbell P.L., Bland-Hawthorn J., 2002, *MNRAS* **329**, 759
- Lozinskaya T.A., Moiseev A.V., Podorvanyuk N.Yu., 2003, *Astronomy Letters* **29**, 77; astro-ph/0301214
- Lozinskaya T.A., Moiseev A.V., Avdeev V.Yu., Egorov O.V., 2006, *Astronomy Letters* **32**, 361; astro-ph/0605189
- Lozinskaya T.A., Moiseev A.V., Podorvanyuk N.Yu., Burenkov A.N., 2008, *Astronomy Letters* **34**, 217; arXiv:0803.2435 [astro-ph]
- Martínez-Delgado I., Tenorio-Tagle G., Muñoz-Tuñón C., et al., 2007, *AJ* **133**, 2892
- Moiseev A.V., 2002, *Bull. SAO* **54**, 74; astro-ph/0211104 (Paper I)
- Movsessian T.A., Magakian T.Yu., Bally J., et al., 2007, *A&A* **470**, 605
- Muñoz-Tuñón C., Gavryusev V., Castoneda H.O., 1995, *AJ* **110**, 1630
- Relaño M., Beckman J.E., 2005, *A&A* **430**, 911
- Rozas M., Zurita A., Beckman J.E., Pérez D., 2000, *A&AS* **142**, 259